

Understanding the Effects of Primary and Secondary Doping via Post-Treatment of P-Type and N-Type Hybrid Organic–Inorganic Thin Film Thermoelectric Materials

Rodrigo Rubio-Govea, Roberto Félix, Regan G. Wilks, Marcus Bär, and Katherine A. Mazzio*

Hybrid organic/inorganic materials have emerged as promising thermoelectric (TE) materials since they inherit the individual strengths of each component, enabling rational materials design with enhanced TE performance. The doping of hybrid TE materials via post-treatment processes is used to improve their performance, but there is still an incomplete understanding of the elicited effects. Here, the impact of different doping methods on the thin film TE performance of p-type Te/poly(3,4-ethylenedioxythiophene):poly(styrene sulfonate) (PEDOT:PSS) and n-type Ag₂Te/PEDOT:PSS hybrid materials is investigated. Primary doping through acid–base and charge transfer processes using H₂SO₄ and tetrakis(dimethylamino)ethylene, respectively, and the effects of secondary doping using ethylene glycol is examined. Through a combination of Hall effect measurements, hard X-ray photoelectron spectroscopy, and Raman spectroscopy, variations in the charge carrier concentration, mobility, and overall TE performance are related to the morphological and chemical structure of the hybrid materials. This study provides an improved understanding of the effects that different post-treatments have on hybrid materials and shows that the impact of these post-treatments on pure PEDOT:PSS does not always apply to hybrid systems. These new insights into post-treatment effects on hybrid materials is expected to facilitate further enhancement of their performance as electronic materials in general and thermoelectric materials in particular.

of clean energy. In recent years, there has been considerable progress in the development of conducting polymers (CPs) for TE applications and the performance of p-type CPs is comparable to that of inorganic TE materials.^[1–3] Despite their promise, one critical issue with the implementation of organic TE materials is that they tend to exhibit inefficient n-doping and unstable electron transport in most n-type polymers, significantly limiting their application, as both efficient p-type and n-type materials with comparable performance are required for practical TE applications.^[4–6] Thereby, further development of efficient n-type materials is needed for the advancement of the field.


During the last decade, composite and hybrid organic/inorganic materials have been developed in an attempt to mitigate the difficulties of enhancing the TE performance arising from the interrelation of the electrical conductivity (σ), Seebeck coefficient (S), and thermal conductivity (κ) through the charge carrier concentration (n).^[7] These hybrid systems can not only inherit the individual strengths of each component, such as the high σ

and S of inorganic materials and the low κ of organic materials, but they also possess interesting interfacial effects at the soft-hard interface that enables decoupling of the thermal and electrical transport, offering the opportunity

1. Introduction

Thermoelectric (TE) materials that can directly interconvert heat and electricity are promising candidates for the production

R. Rubio-Govea, R. Félix, R. G. Wilks, M. Bär, K. A. Mazzio
 Helmholtz-Zentrum Berlin für Materialien und Energie GmbH
 Hahn-Meitner-Platz 1, 14109 Berlin, Germany
 E-mail: katherine.mazzio@helmholtz-berlin.de

 The ORCID identification number(s) for the author(s) of this article can be found under <https://doi.org/10.1002/aelm.202300076>.

© 2023 The Authors. Advanced Electronic Materials published by Wiley-VCH GmbH. This is an open access article under the terms of the Creative Commons Attribution License, which permits use, distribution and reproduction in any medium, provided the original work is properly cited.

R. Rubio-Govea, K. A. Mazzio
 Humboldt-Universität zu Berlin
 Department of Chemistry
 Brook-Taylor-Str. 2, 12489 Berlin, Germany

M. Bär
 Friedrich-Alexander-Universität Erlangen-Nürnberg
 Department of Chemistry and Pharmacy
 Egerlandstr. 3, 91054 Erlangen, Germany

M. Bär
 Helmholtz-Institute Erlangen-Nürnberg for Renewable Energy
 Albert-Einstein-Str. 15, 12489 Berlin, Germany

DOI: 10.1002/aelm.202300076

to rationally design materials with high figures of merit ($zT = \sigma S^2 T \kappa^{-1}$).^[8–10]

In particular, hybrid materials composed of tellurium (Te) nanowires (NWs) embedded in poly(3,4-ethylenedioxythiophene):poly(styrenesulfonate) (PEDOT:PSS) have been prominently studied after Yee et al. reported that their TE performance could be tuned by varying the length of the NWs and modulating the amount of PEDOT:PSS incorporated into the system. In this way, they were able to achieve a power factor (PF = σS^2) close to $100 \mu\text{W m}^{-1} \text{K}^{-1}$.^[8,11] Furthermore, this system offers the opportunity to modulate the composition of Te NWs by having a controlled growth of heterostructures within the Te/PEDOT:PSS hybrid through a simple aqueous technique.^[12]

In this regard, we demonstrated the production of high-performing p-type and n-type $\text{Ag}_x\text{Te/PEDOT:PSS}$ hybrids from the same Te/PEDOT:PSS parent material by varying the silver molar ratio added to the reaction.^[13] In this work, we synthesized n-type $\text{Ag}_2\text{Te/PEDOT:PSS}$ materials with good performance. We determined that the majority charge carrier concentration transitions from holes (h^+) to electrons (e^-) as a result of transport in the NWs and the inclusion of PEDOT:PSS substantially increases the conductivity. Nevertheless, further investigations are needed to enhance the performance of the n-type $\text{Ag}_2\text{Te/PEDOT:PSS}$ hybrid material to bring its PF to values near those of its p-type counterpart.

It is well established in the literature that the overall TE performance of CPs can be considerably enhanced when subjected to post-treatment processes with different solvents.^[14–18] The electronic and optical properties of CPs are related to the formation of polarons and bipolarons that represent single and double charged quasiparticles, respectively.^[19] It is generally accepted that the transport properties strongly depend on the creation of polaron/bipolaron clusters dispersed through the polymer matrix and that their concentration and mobility are dependent on the oxidation level and the degree of crystalline (lamellar) domains.^[20,21] To that end, there are two main categories of post-treatment used to alter the electronic and optical properties of CPs.

The first category, denoted as chemical or primary doping, can be achieved by two processes: 1) A charge transfer (CT) process that relies on the addition of a redox active molecule like tetrakis(dimethylamino)ethylene (TDAE) to the CP, where the doping mechanism is based on a CT process between donor and acceptor. This modifies the charge carrier density of the CP. 2) An acid–base (A^+B^-) process that relies on adding a protonic acid, such as sulfuric acid (H_2SO_4), where the protons released by the acid can enter the backbone of the polymer without modifying the number of electrons present, but the number of positive charges can be increased.^[22–26] The second category, regarded as secondary doping, relies on the addition of a polar solvent (e.g., dimethyl sulfoxide or ethylene glycol (EG)) that only affects the morphological conformation (crystallinity) of the CP chains, and therefore the mobility, without affecting their oxidation level.^[20,21,27]

The most commonly employed method for following changes in the oxidation level of PEDOT is ultraviolet-visible-near infrared (UV–vis–NIR) spectroscopy, as it provides a good understanding of the majority of charge carriers (polarons or bipolarons) present in the structure.^[19,28] However, when

PEDOT-based hybrid materials are investigated, their UV–vis–NIR spectra can be complex, and the PEDOT signature can be masked by strong absorption from the inorganic component, making it necessary to implement different techniques for their characterization. X-ray photoelectron spectroscopy (XPS) is a suitable alternative as it provides information about the doping level via the intensity ratio between PEDOT and the stabilizing counter-ion.^[14,29] Nevertheless, when determining the doping level through XPS, one has to consider the nature of the counter-ion used to stabilize PEDOT, since the information obtained could indicate only the quantity of the counter-ion and not the oxidation level of PEDOT.^[30] For instance, when a polymeric counter-ion (e.g., PSS) is used, a small portion of negatively charged sulfonate groups (PSS^-) may not interact with PEDOT chains, instead interacting with, e.g., impurities such as Na^+ . In this case, all of the PSS^- would contribute to the respective XPS signal intensity, but not all would contribute to the doping effect. On the other hand, when a small counter-ion (e.g., tosylate (Tos)) is used, only the amount necessary to neutralize the doping charge in PEDOT is introduced into the system, and a change in their intensity ratio is directly related to the oxidation level.^[14,31] Additionally, Raman spectroscopy is a powerful complementary characterization technique as it provides information about the structural arrangement of molecular systems and their chemical surroundings.^[32] It has been shown that the doping level of PEDOT can be approximately estimated by following the changes of the Raman mode associated with the $\text{C}_\alpha=\text{C}_\beta$ symmetric stretching mode of the five-membered thiophene ring. This signal is known to redshift as the oxidation level decreases.^[33–37]

Even though there are many reports in the literature focused on analyzing the effects of post-treatment on the TE performance of pure PEDOT systems,^[20,21,23,26,38–41] there is a lack of systematic analysis of the effects of post-treatments on PEDOT-based hybrid organic/inorganic materials. In this work, we investigate the impacts of primary and secondary doping on the performance of p-type Te/PEDOT:PSS and n-type $\text{Ag}_2\text{Te/PEDOT:PSS}$ hybrid TE materials in their thin-film configuration through application of TDAE, H_2SO_4 , and EG post-treatments. By analyzing the materials with a combination of transmission electron microscopy (TEM), X-ray diffraction (XRD), Raman spectroscopy, hard X-ray photoelectron spectroscopy (HAXPES), and Hall measurements, we determine the impact that the post-treatments have on the morphological and chemical structure of the PEDOT:PSS constituent, as well as details and changes to the composition of the inorganic component. This study provides an improved understanding of the effects that post-treatments have on hybrid electronic materials, which will enable further enhancement of their thin film TE performance.

2. Results

2.1. Synthesis and Structural Characterization

To synthesize Te/PEDOT:PSS and $\text{Ag}_2\text{Te/PEDOT:PSS}$ NWs, we performed a two-step synthetic procedure, in which hybrid Te/PEDOT:PSS NWs are synthesized in the first step and then

AgNO₃ is added in the second step in order to transform the Te/PEDOT:PSS into Ag₂Te/PEDOT:PSS NWs. XRD results (Figure S1a, Supporting Information) confirm the successful synthesis and transformation of hexagonal Te/PEDOT:PSS NWs into monoclinic Ag₂Te/PEDOT:PSS NWs without any residual unreacted Te. However, we observe diffraction signals corresponding to elemental hexagonal and cubic Ag. As seen from TEM, the Te/PEDOT:PSS hybrid material exhibits an elongated NW morphology and is generally single crystalline with a length/diameter aspect ratio of ≈26 (Figure S1b, Supporting Information). After the second step of the synthesis, there is an evident change in morphology as the NWs pass from a rigid Te structure to a curved Ag₂Te structure (Figure S1c, Supporting Information). A detailed description of the transition from Te to Ag₂Te as the Ag molar ratio is increased can be found in ref. [13]. The TEM images represent the pristine hybrid materials, which were deposited as films. The p-type Te/PEDOT:PSS and n-type Ag₂Te/PEDOT:PSS were subsequently exposed to different post-treatment processes with TDAE, H₂SO₄, or EG.

2.2. Thermoelectric Characterization

To evaluate the effect that the post-treatment through both primary and secondary doping has on the TE properties of the hybrid materials, each pristine sample was first evaluated by measuring two heating/cooling cycles between 20 and 120 °C. They were then subjected to different post-treatment

processes and measured again in the same temperature region. **Figure 1** shows an example of the TE characterization of Ag₂Te/PEDOT:PSS in its pristine state and after post-treatment with a few drops of the redox-active molecule TDAE (TDAE_(d)). The complete TE characterization of all samples with the different post-treatments can be found in Figures S2–S8 in the Supporting Information. The details of thermoelectric measurement error calculations and accompanying discussion can be found in the Supporting Information. From the changes observed in σ , S , κ , PF, and zT , the percentage variations relative to the pristine values were calculated. **Figure 2a–c** shows the σ , S , and κ percentage variations, respectively, for all samples and all post-treatment methods used. Since the percentage variations remain mostly constant throughout the whole temperature range, Figure 2 only reports the percentage variations at 20 °C. The complete percentage variations covering the entire investigated temperature range can be found on Figure S10 in the Supporting Information. From this point onward, we will focus only on the three main TE properties (σ , S , and κ) and not discuss the PF and zT variations, as they depend on the variations obtained from σ , S , and κ .

2.2.1. Electrical Conductivity (σ) Variations

A summary of the percentage variations of the electrical conductivity after the different post-treatments can be found in Figure 2a. It can be seen that the H₂SO₄ post-treatment

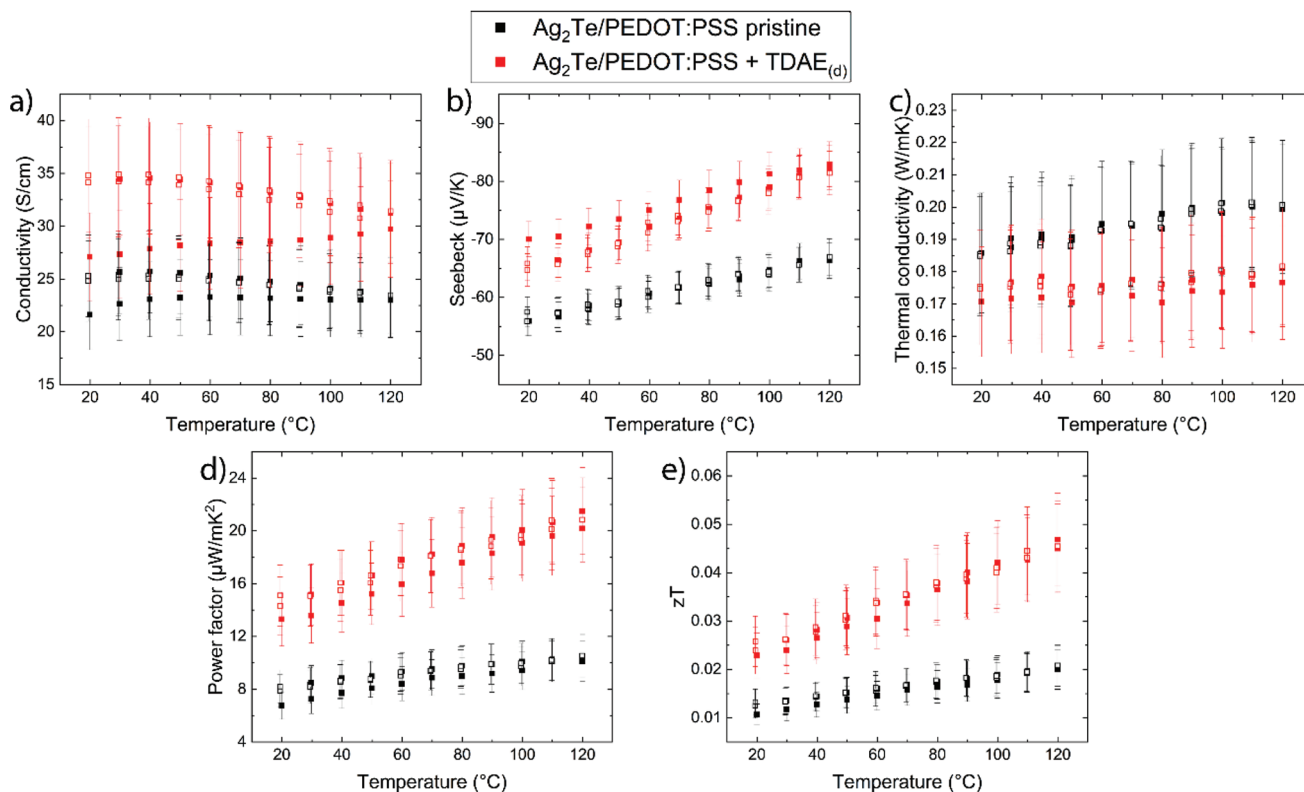


Figure 1. Thermoelectric characterization of pristine and TDAE_(d) post-treated Ag₂Te/PEDOT:PSS. a) Electrical conductivity, b) Seebeck coefficient, c) thermal conductivity, d) power factor, and e) zT for two heating/cooling cycles between 20 and 120 °C. Filled squares correspond to heating cycles and open squares correspond to cooling cycles.

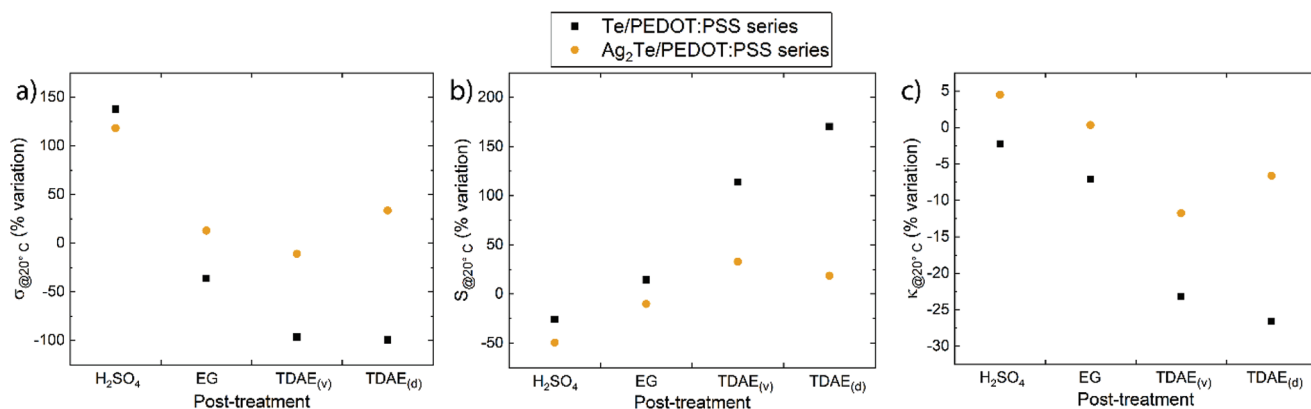


Figure 2. a) Conductivity, b) Seebeck coefficient, and c) thermal conductivity percentage variations at 20 °C for Te/PEDOT:PSS (black) and Ag₂Te PEDOT:PSS (gold) samples post-treated with H₂SO₄, EG, and TDAE.

presents a pronounced σ enhancement for both hybrid systems of $\approx 140\%$ and 120% for Te/PEDOT:PSS and Ag₂Te/PEDOT:PSS, respectively. In contrast, in the case of EG post-treatment, the σ of the Te/PEDOT:PSS sample suffered a 40% decrease, while that of the Ag₂Te/PEDOT:PSS sample was increased by 10% after EG post-treatment. The results of the H₂SO₄ post-treatment are expected, as it is known that acid–base doping can increase the charge carrier concentration. However, the EG post-treatment results are not as expected, as it is known that for pure PEDOT:PSS, secondary doping with EG can increase σ by two orders of magnitude.^[39]

When the Ag₂Te/PEDOT:PSS sample was treated with a few drops of TDAE (TDAE_(d)), its σ increased by 35%, and surprisingly, when treated with TDAE vapor (TDAE_(v)), the σ was decreased by 15%. We posit that the discrepancy in σ variations may be caused by the penetration depth of the dopant within the polymer domain of the hybrid material according to the different post-treatment methods used. To corroborate that the reduction of PEDOT:PSS differs within the TDAE_(v) and TDAE_(d) post-treatment, we post-treated Te/PEDOT:PSS with TDAE_(v) and TDAE_(d). As seen on Figure S4 in the Supporting Information, the σ of the TDAE_(v) post-treated Te/PEDOT:PSS sample decreased from 13.13 ± 1.25 to 0.48 ± 0.04 S cm⁻¹, and when it was treated with TDAE_(d) (Figure S5, Supporting Information) it decreased from 18.5 ± 1.84 to 0.14 ± 0.01 S cm⁻¹, corresponding to a 95% and 99% decrease, respectively. The drastic decrease of σ is attributed to the reduction of PEDOT by TDAE_(v) and TDAE_(d) since the electronic transport of the Te/PEDOT:PSS hybrid occurs predominantly through the PEDOT:PSS component.^[42] This is supported *vide infra* with Hall measurements.

In our previous work, we demonstrated that if the PEDOT:PSS portion is replaced by polyvinylpyrrolidone (PVP), the Ag_xTe/PVP hybrids have limited conductivities while the Te/PEDOT:PSS hybrids have similar conductivity values to that of neat PEDOT:PSS. This demonstrates that the inorganic component of the hybrids only has a small contribution to σ .^[13] Based on this, we attribute the observed σ variations to changes to the oxidation level and morphological conformation of the PEDOT:PSS fraction of the hybrids, as will be discussed in Section 3.

2.2.2. Seebeck Coefficient (S) Variations

Figure 2b shows the percentage variations of S for all post-treated samples. Of the post-treatment methods employed, Te/PEDOT:PSS samples post-treated with EG, TDAE_(v), and TDAE_(d) resulted in an increased $|S|$ by 15%, 110%, and 175%, respectively. Also the Ag₂Te/PEDOT:PSS samples post-treated with TDAE_(v) and TDAE_(d) resulted in an increased $|S|$ by $\approx 25\%$. In contrast, the Te/PEDOT:PSS sample post-treated with H₂SO₄ resulted in a 25% decrease in $|S|$, and the Ag₂Te/PEDOT:PSS samples post-treated with EG and H₂SO₄ resulted in a decreased $|S|$ by 10% and 50%, respectively. An increase in the $|S|$ is known to correlate with a decrease in the charge carrier concentration, n , and vice versa.

2.2.3. Thermal Conductivity (κ) Variations

Figure 2c shows the variations of κ for all post-treated samples. For the Te/PEDOT:PSS samples treated with H₂SO₄ and EG and all of the Ag₂Te/PEDOT:PSS samples, the variations of κ are within the instrumental error given by the manufacturer (10%).^[43] However, Yang et al. demonstrated that the thermal conductivity of Te/PEDOT:PSS hybrids is dominated by the inorganic portion and that the electrical conductivity is dominated by PEDOT:PSS, making it possible to decouple charge and heat transport,^[42] which is the reason we do not observe an increase of κ after increasing the σ of our hybrids. In the case of the Te/PEDOT:PSS samples, the post-treatment with TDAE_(v) and TDAE_(d) resulted in a decrease of κ by 25% and 30%, respectively, which can be explained by the drastic decrease (96% and 99%, respectively) of σ , which in turn decreases the electronic contribution to κ .

2.2.4. Hall Effect Measurements

The variations observed in σ , S , and κ can be explained by changes induced in the charge carrier concentration and mobility (n and μ , respectively) by the different post-treatment methods. It is well known that σ and κ follow a direct relation

Table 1. Charge carrier concentrations (n) and mobilities (μ) obtained by Hall measurements for the pristine and post-treated Te/PEDOT:PSS and Ag₂Te/PEDOT:PSS samples at 20 °C. Thickness values used for the calculation of n correspond to the pristine samples and the sample thickness was not observed to be affected by the post-treatments. Negative n values correspond to electrons (e^-) and positive values correspond to holes (h^+).

Sample	Thickness [nm]	Treatment ^{a)}	Pristine		Post-treated	
			n [$\times 10^{19}$ cm ⁻³]	μ [cm ² V ⁻¹ s ⁻¹]	n [$\times 10^{19}$ cm ⁻³]	μ [cm ² V ⁻¹ s ⁻¹]
Te/PEDOT:PSS	229 ± 62	H ₂ SO ₄	15.74 ± 4.24	0.78 ± 0.30	188.95 ± 51.65	0.15 ± 0.06
	933 ± 136	EG	11.22 ± 1.64	0.40 ± 0.08	12.12 ± 1.77	0.22 ± 0.05
	1205 ± 115	TDAE _(v)	10.88 ± 1.04	0.51 ± 0.07	0.43 ± 0.04	0.45 ± 0.06
	334 ± 70	TDAE _(d)	12.75 ± 1.27	0.62 ± 0.09	0.01 ± 0.002	2.18 ± 0.04
Ag ₂ Te/PEDOT:PSS	2332 ± 293	H ₂ SO ₄	-1.22 ± 0.15	11.20 ± 1.99	-4.14 ± 0.52	7.55 ± 1.34
	1607 ± 155	EG	-0.87 ± 0.08	16.78 ± 2.30	-1.12 ± 0.11	14.73 ± 2.02
	1511 ± 193	TDAE _(v)	-0.75 ± 0.10	16.67 ± 3.01	-0.59 ± 0.08	20.50 ± 3.71
	1292 ± 198	TDAE _(d)	-1.20 ± 0.18	13.00 ± 2.82	-0.79 ± 0.12	28.25 ± 6.12

^{a)}Sulfuric acid (H₂SO₄), ethylene glycol (EG), tetrakis(dimethylamino)ethylene vapor (TDAE_(v)) and drop (TDAE_(d)).

to n , while S presents an inverse relation to n .^[7] To understand the changes of σ , S , and κ after post-treatment, Hall effect measurements were conducted on the pristine and post-treated samples to follow changes in n and μ ; Table 1 summarizes the results obtained. Representative raw data from Hall effect measurements are presented on Appendix S1 in the Supporting Information.

As seen in Figure 3a,b, the post-treatments follow the same trend in both Te/PEDOT:PSS and Ag₂Te/PEDOT:PSS samples. In the case of the H₂SO₄ post-treatment, both samples present an increased n and a decreased μ . For the EG post-treatment, the n of both samples is slightly increased, however, the difference is within the experimental uncertainty. Similarly, the μ of both samples is decreased, with a more pronounced decrease for the Te/PEDOT:PSS sample.

In the case of TDAE_(v) post-treatment, the Te/PEDOT:PSS sample shows a substantial decrease of n , while its μ remains constant. For the Ag₂Te/PEDOT:PSS it appears that there is a decrease of n and an increase of μ ; however, the observed differences are within experimental uncertainty. The effects of the TDAE_(d) post-treatment are similar to those of the TDAE_(v) for both samples. The n of Te/PEDOT:PSS sample is greatly decreased while the μ is enhanced. For the Ag₂Te/PEDOT:PSS sample, similarly to the TDAE_(v) post-treatment, the variation of n is within error. In this case, there is a pronounced increase of μ .

2.3. HAXPES Characterization

2.3.1. Effect of Post-Treatment on Te and Ag₂Te NWs

HAXPES allows probing of the chemical, electronic, and molecular structure near the surface of a material. As this technique entails irradiating the probe with X-rays to excite photoelectrons, special measures were taken to prevent degradation of the light-sensitive organic component of the samples during this process (see the Experimental Section for more details). The HAXPES survey spectra of the pristine and post-treated Te/PEDOT:PSS and Ag₂Te/PEDOT:PSS samples, as well as some reference compounds, are presented in Figure S11 in the Supporting Information and are used to investigate the elemental composition near the surface of the samples. As expected, the spectra of the Te/PEDOT:PSS samples consist mainly of signature Te-, C-, O-, and S-derived lines. In addition to these core levels, the spectra of the Ag₂Te/PEDOT:PSS samples show Ag-related signals. (Detailed spectra of the C 1s, O 1s, N 1s, and Ag 3d for these sample series are found in Figures S12 and S13, Supporting Information).

To evaluate any compositional changes induced by post-treatments of the Te and Ag₂Te, the energy region of the (Ag 3p/) Te 3d core levels of the Te/PEDOT:PSS and Ag₂Te/PEDOT:PSS hybrids were analyzed in detail and are shown in Figure 4a,b,

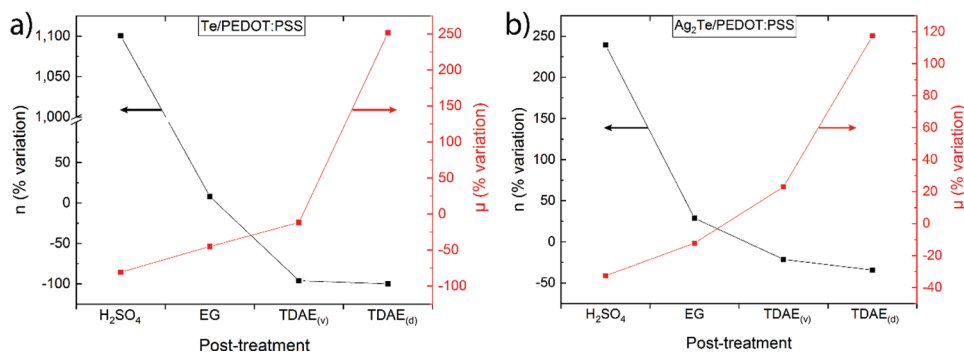


Figure 3. Charge carrier density (n , black) and mobility (μ , red) percentage variations at 20 °C for a) Te/PEDOT:PSS and b) Ag₂Te PEDOT:PSS samples post-treated with H₂SO₄, EG, and TDAE.

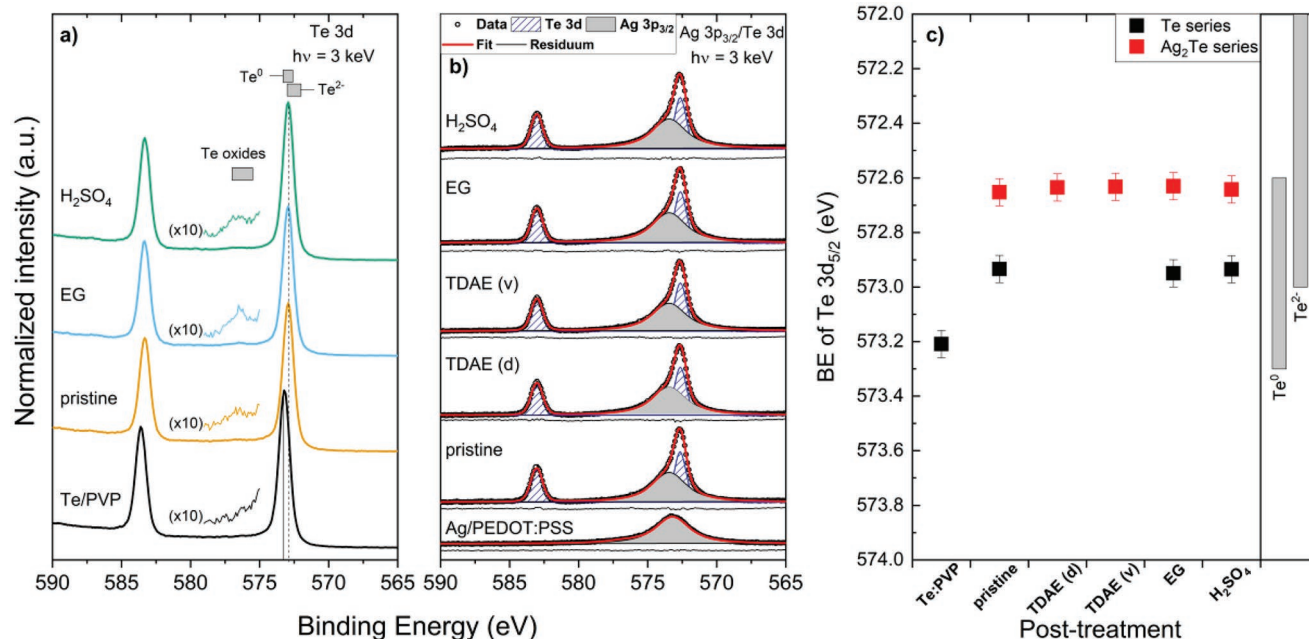


Figure 4. HAXPES spectra of the a) Te 3d and b) Ag 3p_{3/2}/Te 3d energy regions of pristine and variously post-treated Te/PEDOT:PSS and Ag₂Te/PEDOT:PSS samples, respectively. Curve fit results are included in (b). Determined BE values of the c) Te 3d_{5/2} lines of the investigated samples. Spectra are normalized to background intensity, with vertical offsets added for clarity. BE ranges of Te 3d_{5/2} for reference compounds reported in the literature are shown as gray-filled boxes in (a) and (c).^[45] In (a), a BE range has been magnified (x10, inset) for all spectra to make the detected (minor) secondary Te contribution more apparent.

respectively. The binding energy (BE) values determined for the Te 3d_{5/2} core levels are presented in Figure 4c. From here, it can be seen that the BE for the pristine Te/PEDOT:PSS sample is 572.93 ± 0.05 eV, corresponding to a Te⁽⁰⁾-like chemical environment;^[44] the fact that the BE does not change after post-treatment indicates that the chemical state is not significantly affected. A minor signal can be detected in the spectra of all Te/PEDOT:PSS samples at a BE of 576.6 ± 0.1 eV (see Figure 4a), which can be attributed to Te oxides.^[45] However, due to the low intensity of this contribution [i.e., 2% ± 1% of the total Te 3d signal] and the air exposure of samples during preparation and post-treatment steps (see the Experimental Section for more details), no direct conclusions can be drawn regarding the effect of the post-treatments on the formation of this (minor) Te chemical species. Additionally, we analyzed a reference Te/PVP sample to assess the effect that the nature of the polymer has on the organic/inorganic interface. As seen in Figure 4c, the BE of the Te 3d_{5/2} of the Te/PVP sample is found at 573.21 ± 0.05 eV. We posit that this 0.3 eV shift toward higher BE of the Te/PEDOT:PSS samples is due to the formation of an electron-rich interface, supporting the notion of the templating effect model proposed by Kumar et al.^[10] A detailed discussion regarding the templating effect is given below in the discussion section.

In the case of the Ag₂Te/PEDOT:PSS, all samples have a Te 3d_{5/2} BE of 572.64 ± 0.05 eV, as shown in Figure 4c, which is consistent with reported values for Ag₂Te nanocrystals;^[46] the Ag 3p_{3/2} line for these samples is found at a BE of 573.44 ± 0.05 eV, corresponding to Ag⁺ present in Ag₂Te.^[13] Moreover, based on the measured Ag 3p/Te 3d spectra, all Ag₂Te/PEDOT:PSS samples showed an HAXPES-derived [Ag]:[Te] composition ratio

of 2:1, consistent with the nominal stoichiometry of the NWs (Figure S14, Supporting Information). Together, these results indicate that the post-treatments do not modify the chemical composition of the Ag₂Te NWs substantially (note: Differences in the O 1s, Ag 3d, and C 1s energy regions of the investigated Ag₂Te/PEDOT:PSS samples were detected. For more details, see Figure S13, Supporting Information).

2.3.2. Effect of Post-Treatment on PEDOT:PSS

To confirm compositional changes induced by post-treatments on the PEDOT:PSS component of the hybrid materials, the S 1s core level was investigated via HAXPES. Figure 5 shows the S 1s spectra for pristine and post-treated Te/PEDOT:PSS (Figure 5a) and Ag₂Te/PEDOT:PSS (Figure 5b) samples, along with curve fit results. The chemical structure of PEDOT:PSS gives rise to three main S 1s signals, corresponding to the sulfonic acid (PSSH) at 2477.70 ± 0.05 eV, the sulfonate anion (PSS⁻) at 2477.55 ± 0.05 eV, and the thiophene ring at 2471.62 ± 0.05 eV.^[47] By evaluating the intensity of these signals, i.e., (thiophene)/[(PSSH) + (PSS⁻)], it is possible to determine the approximate PEDOT-to-PSS ratio near the surface of the investigated samples by HAXPES. As seen in Figure 5a, when the pristine Te/PEDOT:PSS hybrid is formed, the thiophene peak intensity is greater than that of the pure PEDOT:PSS signal, indicating that during the synthesis procedure there is an intrinsic removal of PSS, changing the PEDOT-to-PSS ratio from (0.42 ± 0.05) to (0.67 ± 0.05), as shown in Figure 5c. When Te/PEDOT:PSS is post-treated with EG, the PEDOT-to-PSS ratio is increased to (0.89 ± 0.05) indicating a greater removal

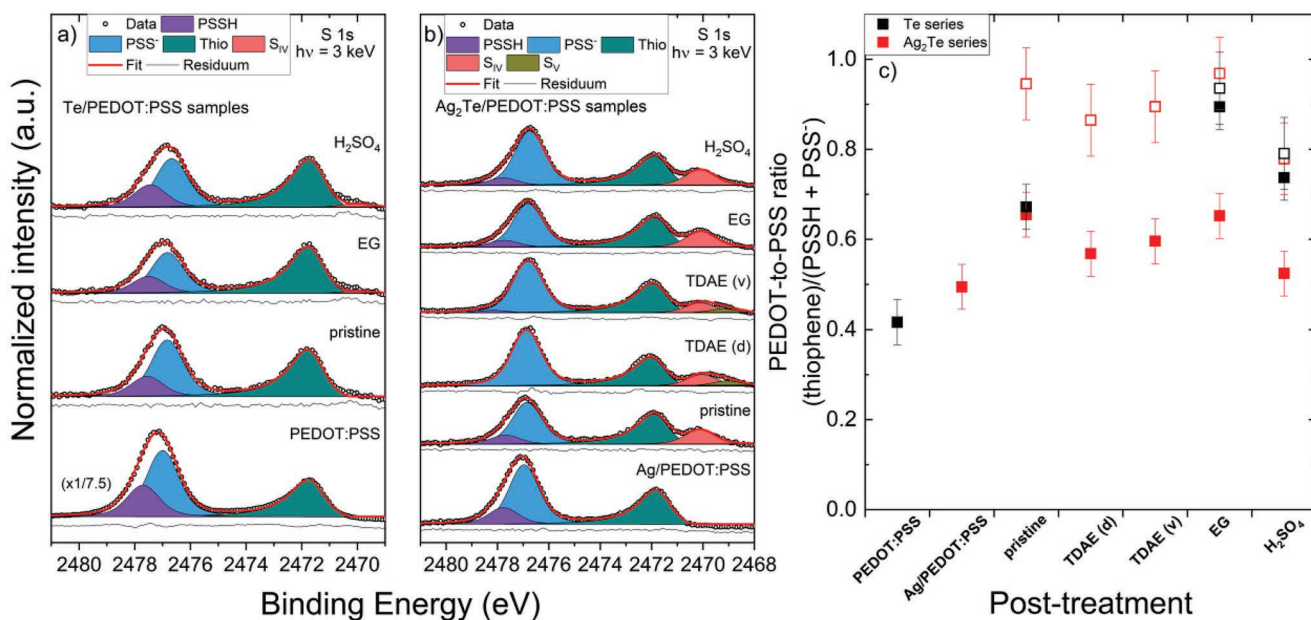


Figure 5. HAXPES spectra of the S 1s energy region of pristine and variously post-treated a) Te/PEDOT:PSS and b) Ag₂Te/PEDOT:PSS samples, including curve fit results. c) Surficial HAXPES-determined PEDOT-to-PSS ratio of the investigated samples, the open symbols correspond to the calculated PEDOT-to-PSS ratios considering signals S_{IV} and S_V as thiophene contributions.

of PSS. When it was post-treated with H₂SO₄, the PEDOT-to-PSS ratio is (0.74 ± 0.05) , signifying that only a small portion of PSS is removed by H₂SO₄. Moreover, for the EG and H₂SO₄ post-treated samples, there is an additional (minor) peak at 2470.00 ± 0.05 eV (S_{IV}). While there is limited literature containing HAXPES S 1s data from reference compounds, due to the BE position of this minor peak, we can infer that it most likely results from a species in which S has a -2 oxidation state.^[48,49] The origin of this signal is discussed further *vide infra*.

As seen in Figure 5b, the intensity of the thiophene peak of the pristine Ag₂Te/PEDOT:PSS sample remains unchanged relative to the pristine Te/PEDOT:PSS from the first part of the synthesis, having a PEDOT-to-PSS ratio of (0.65 ± 0.05) (Figure 5c). The constant ratio indicates that there is no further decrease of the PSS content during the second step of the synthesis. Similarly, when the Ag₂Te/PEDOT:PSS sample is post-treated with EG, the PEDOT-to-PSS ratio remains unchanged, indicating that there is no further decrease in the PSS content. When it is post-treated with H₂SO₄, there is an apparent increase of the PSS content, resulting in a PEDOT-to-PSS ratio of (0.52 ± 0.05) . At first glance, these results suggest that the effect of EG and H₂SO₄ post-treatments are different for the Te/PEDOT:PSS and Ag₂Te/PEDOT:PSS samples. Nevertheless, the calculated PEDOT-to-PSS ratios change when considering the contributions of signals S_{IV} and S_V (BE 2469.1 ± 0.05 eV), as will be discussed in the following section.

When the Ag₂Te/PEDOT:PSS sample was treated with TDAE_(v), the PEDOT-to-PSS ratio was slightly reduced to (0.60 ± 0.05) and the contribution of the PSSH peak is greatly reduced, leaving the majority of the PSS in its PSS⁻ form. Moreover, when it was treated with TDAE_(d) the PEDOT-to-PSS ratio was further reduced to (0.57 ± 0.05) and the PSS portion only has a contribution from the PSS⁻ form, as the signal from the PSSH

is completely diminished. Additionally, for both TDAE_(v) and TDAE_(d) post-treatment, the thiophene signal is slightly shifted toward higher BE (Δ BE ≈ 0.15 eV), indicating a modification of the oxidation level of PEDOT, similar to the results of Bubnova et al. for PEDOT:Tos samples treated with TDAE.^[14] Furthermore, all of the Ag₂Te/PEDOT:PSS samples show an S_{IV} signal at 2470.10 ± 0.05 eV in significantly higher intensity compared to the Te/PEDOT:PSS series and, in the case of TDAE post-treated Ag₂Te/PEDOT:PSS samples, there is an additional contribution at BE 2469.1 ± 0.05 eV (i.e., peak S_V), indicating the presence of additional sulfur contributions with -2 oxidation states.

The origin of signals S_{IV} and S_V is not fully understood and the following mechanisms can be proposed:^[48]

1. Some thiophene groups are chemisorbed onto the surface of the NWs.
2. Thiol groups are formed via thiophene ring-opening or the reduction of SO₃ and are physisorbed and/or chemisorbed onto the surface of the NWs.

According to Okamoto et al.,^[48] the peak at 2470.1 eV may arise from the interaction of thiols formed by either the cleavage of the thiophene ring or the reduction of SO₃ with Ag₂Te, and the peak at 2469.1 eV may arise from the interaction of the thiols with elemental Ag nanoparticles. However, when Ag NPs were synthesized without the presence of Te, the S 1s spectrum of Ag/PEDOT:PSS (Figure 5b) does not show the additional S_{IV} and S_V peaks. Additionally, we were not able to observe the characteristic Raman signals that would be expected to arise from thiols absorbed on Ag surfaces between 650 and 700 cm⁻¹ (data not shown).^[50] Based on this, we propose another plausible origin of the S_{IV} and S_V peaks.

In the first step of the synthesis, during the growth of the Te NWs, PEDOT:PSS acts as a structure directing agent that

promotes the formation of the NWs. According to molecular dynamics (MD) simulations and density functional theory (DFT) calculations done by Kumar et al.,^[10] due to the higher interaction energy of PEDOT over PSS with the NWs surface, PEDOT chains tend to self-align in a planar configuration at the NW surface promoting the formation of an electron-rich interface, and causing an electron density transfer from π orbitals to σ orbitals in the PEDOT. We posit that during the electron rearrangement, the S atom of the thiophene ring becomes more readily available to interact with the surface of the NWs, causing the appearance of the additional S_{IV} contribution, which corresponds to the thiophene ring with modified electronic density rather than the cleavage of the ring and formation of thiols. In other words, the S_{IV} species relates to the polymer directly at the nanowire interface.

During the formation of Ag_2Te during the second step of the synthesis, the templating effect is maintained, which is why we also observe the presence of the S_{IV} signal in these samples. We theorize that the reason for the increased intensity of the S_{IV} signal for all the Ag_2Te /PEDOT:PSS samples is that the absorption energy of PEDOT on the Ag_2Te surface is greater than the absorption energy on Te. A similar phenomenon was reported for PEDOT on $Cu_{1.75}Te$ versus Te.^[10] This theory is supported by the appearance of a minor shoulder detected for all post-treated Ag_2Te /PEDOT:PSS samples on the Ag $3d_{5/2}$ spectra at BE ≈ 368 eV (see Figure S13c, Supporting Information), which suggests the formation of new Ag–S and/or Ag–O bonds. Furthermore, we stipulate that the S_V signal observed for only the TDAE_(v) and TDAE_(d) post-treated samples correspond to the thiophene moieties interacting with residual TDAE, as no other samples show this additional contribution. The presence of residual TDAE on the post-treated samples is confirmed by the N 1s spectra (Figure S13b, Supporting Information), where the peak at 401.33 ± 0.05 eV corresponds to TDAE²⁺.^[51]

By taking into consideration signals S_{IV} and S_V to calculate the PEDOT-to-PSS ratios, we get modified values for the H_2SO_4 and EG post-treated Te/PEDOT:PSS samples, however, the new values are within error of the previous ratios. In contrast, for all of the Ag_2Te /PEDOT:PSS samples, the PEDOT-to-PSS ratios are increased substantially with inclusion of the S_{IV} and S_V species. In the case of the pristine sample, the ratio increases to

(0.95 ± 0.08) indicating that during the second step of the synthesis there is a greater removal of excess PSS. For the TDAE_(v) and TDAE_(d) samples, the values decrease, relative to the pristine sample, to (0.89 ± 0.08) and (0.86 ± 0.08) , respectively. These values are suggestive of an increased phase segregation between PEDOT and PSS. For the EG post-treated sample the ratio remains the same as in the pristine sample, indicating no further removal of excess PSS. For the H_2SO_4 post-treated sample, the ratio decreased to (0.78 ± 0.08) indicating a phase segregation between PEDOT and PSS, similar to that found for the Te/PEDOT:PSS sample. The recalculated PEDOT-to-PSS ratios that include contributions from the S_{IV} and S_V species are represented in Figure 5c as open symbols.

The observed changes near the surface PEDOT-to-PSS ratios are reflected as structural rearrangements of the PEDOT chains induced either by the removal of excess PSS or by phase segregation, causing a change in the degree of crystallinity of the PEDOT chains. To further assess morphological conformation changes of PEDOT:PSS caused by the post-treatment methods and their effect on the TE performance of the hybrids, we performed Raman spectroscopy.

2.4. Raman Characterization

Raman spectroscopy is a sensitive characterization technique that can provide information about changes in the structural arrangement of molecular systems and their chemical surroundings. Our results indicate that variations of the TE properties of p-type Te/PEDOT:PSS and n-type Ag_2Te /PEDOT:PSS after post-treatment arise from compositional and conformational changes of the PEDOT:PSS component, as no apparent changes were observed in the low-frequency region where the signals corresponding to Te and Ag_2Te appear, as shown in Figure S15 in the Supporting Information. To follow conformational changes in PEDOT:PSS induced by the different post-treatments, we first measured a pure PEDOT:PSS sample as reference. As shown in Figure 6a, the most intense band is located at 1430 cm^{-1} and is assigned to the $C_{\alpha}=C_{\beta}$ symmetric stretch of the thiophene ring, and the two bands located at 1536 and 1570 cm^{-1} correspond to the $C_{\alpha}=C_{\beta}$ asymmetric stretch. The band at 1371 cm^{-1} corresponds to the $C_{\beta}-C_{\beta}$ stretch, and

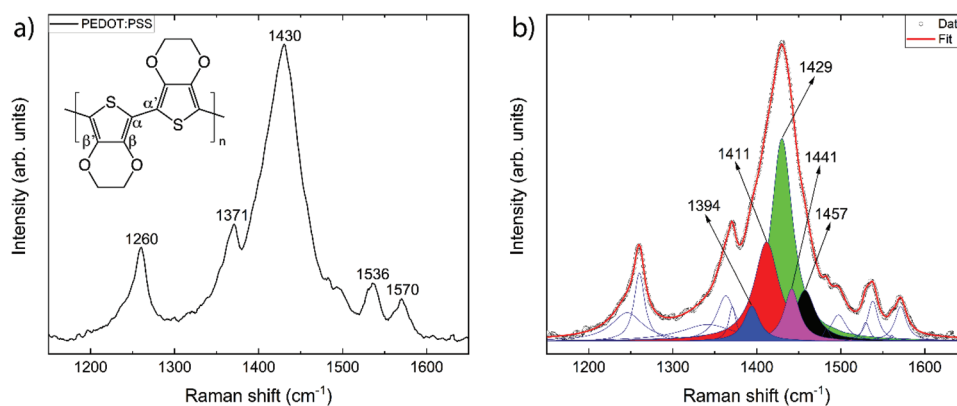


Figure 6. a) Raman spectra of pure PEDOT:PSS. b) Deconvolution of the main $C_{\alpha}=C_{\beta}$ symmetric stretch of pure PEDOT:PSS. The inset on (a) corresponds to the schematic representation of the chemical structure of PEDOT.

the band at 1260 cm^{-1} is attributed to the $C_{\alpha}-C_{\alpha'}$ interring stretching.^[33,52]

The oxidation level of PEDOT can be estimated by the position of the $C_{\alpha}=C_{\beta}$ symmetric stretch. When PEDOT is in its neutral state, the $C_{\alpha}=C_{\beta}$ symmetric stretch appears at $\approx 1415\text{ cm}^{-1}$, and as it gets oxidized, this band blueshifts to 1445 cm^{-1} .^[36,53] In the same manner, the intramolecular delocalization of π electrons along the path defined by the conjugated C=C bonds along the polymer backbone, defined as the effective conjugation length (ECL), is affected by conformational distortions and/or intermolecular interactions.^[54–56] Generally, as the ECL of polythiophenes increases, the collective symmetric vibration of the C–C/C=C skeleton is downshifted.^[57,58] Similarly, a shift toward higher wavenumbers is an indication of the aromatization of PEDOT, suggesting a bipolaronic structure. Based on the HAXPES results in Figure 5a,b, we can infer that changes in the position of the $C_{\alpha}=C_{\beta}$ symmetric stretch of all samples, with exception of the TDAE post-treatments, are mainly due to modifications of the ECL through conformational distortions and/or intermolecular interactions and are not related to changes in the oxidation level of PEDOT as no shifts of the BE associated with the thiophene ring signal were observed.

The main symmetric $C_{\alpha}=C_{\beta}$ stretching band is composed of different contributions of the collective vibrations of PEDOT chains with different ECLs. Generally, vibrational modes related to short ECLs tend to appear at $\approx 1450\text{ cm}^{-1}$ and as the ECL is increased, the vibrations downshift.^[45,46,74] The mixture of different ECLs that gives rise to the main symmetric $C_{\alpha}=C_{\beta}$ peak can be correlated to the charge carrier mobility (μ) of the hybrids. It has been reported for similar polythiophene systems that the ECL and position of the symmetric $C_{\alpha}=C_{\beta}$ peak is related to the chemical structure of the thiophene backbone.^[55,59] As the neutral thiophene is oxidized into a radical cation (polaron), the thiophene oligomer tends to shift from a benzoidal to a quinoidal conformation. As it is further oxidized, the formation of a dication (polaron pair) is promoted, resulting in a full quinoidization of the thienyl backbone due to the strong electrostatic repulsion between the positive charges confined in a relatively small molecule.^[58–60] By deconvoluting the main symmetric $C_{\alpha}=C_{\beta}$ stretching band of the pristine and post-treated Te/PEDOT:PSS and Ag_2Te /PEDOT:PSS samples, it is possible to estimate if the stretching band is composed of one or more ECLs, with the number of deconvoluted peaks corresponding to the number of ECLs in the polymer domain. At the same time, the full width at half maximum (FWHM) of the deconvoluted peaks gives an indication of the crystallinity of the domains, and the relative intensities reflect the contribution of each ECL to the whole.

Figure 6b shows an example of the deconvolution of the symmetric $C_{\alpha}=C_{\beta}$ peak of pure PEDOT:PSS. From here it can be seen that the main vibrational mode can be deconvoluted into five different contributions centered at 1394, 1411, 1429, 1441, and 1457 cm^{-1} . From this, it is evident that the pure PEDOT:PSS film consists of a mixture of different ECLs, having a considerable contribution of short ECLs located at higher wavenumbers.^[61,62] In the same manner, the multiple

contributions of the deconvoluted $C_{\alpha}=C_{\beta}$ asymmetric stretch, $C_{\beta}-C_{\beta}$ stretch, and $C_{\alpha}-C_{\alpha'}$ interring stretching correspond to the same vibrational modes of different sections of the PEDOT chain, e.g., central and terminal thiophene rings, with different ECLs.^[63] Figures showing the deconvoluted Raman spectra of all Te/PEDOT:PSS and Ag_2Te /PEDOT:PSS samples can be found in Figures S16–S25 in the Supporting Information and results from the deconvolution of the main symmetric $C_{\alpha}=C_{\beta}$ peak are summarized in Table 2, and addressed further in the discussion section.

3. Discussion

3.1. Pristine Hybrid Materials

Based on the surface PEDOT-to-PSS ratio derived from the HAXPES measurements, we see that during the synthesis of the pristine Te/PEDOT:PSS, there is an intrinsic removal of excess PSS relative to pure PEDOT:PSS. Additionally, we observed a shift of 0.3 eV of the BE of the Te $3d_{5/2}$ line when PEDOT:PSS was replaced by PVP (Figure 4c). We posit that the observed difference in BE is a direct measurement of the templating effect proposed by Kumar et al.,^[10] where an electron-rich interface is created between the Te NW surface and PEDOT chains, facilitating the planar alignment of the first few layers of PEDOT moieties over the inorganic surface. When the PEDOT:PSS fraction of the hybrid gets replaced by PVP, the so-called pillow effect is suppressed,^[64,65] preventing the formation of the electron-rich interface and shifting the BE of the Te $3d_{5/2}$ of the Te/PVP hybrid to higher values. This result provides experimental evidence of the structural reordering (templating effect) of PEDOT chains that leads to their reorganization at the NW surface. This effect was previously proposed through MD and DFT calculations and highlighted the importance of the electron-rich interface and its role in high TE performance of Te/PEDOT:PSS hybrids.^[10] It is noteworthy to point out that none of the post-treatments disrupted the templating effect as there is no shift of the BE of the Te $3d_{5/2}$ of the Te/PEDOT:PSS samples.

Additionally, there was no apparent change in the PEDOT-to-PSS ratio during the second step of the synthesis, indicating that there is no further reduction of PSS content upon formation of Ag_2Te /PEDOT:PSS hybrids. Nevertheless, when signals S_{IV} and S_V were used to calculate the ratio, there seems to be a great removal of excess PSS. Furthermore, relative to Te/PEDOT:PSS, Ag_2Te /PEDOT:PSS showed a reduction in the number of contributions related to the vibrational mode of the symmetric $C_{\alpha}=C_{\beta}$ peak of the Raman spectrum. This indicates that during the formation of Ag_2Te /PEDOT:PSS there is a favorable morphological modification of the PEDOT chains that reduces the mixture of different ECLs. We speculate that the reduction of the diverse ECLs is related to the higher absorption energy of PEDOT over the Ag_2Te NWs surface relative to Te NWs, causing the modification of the electron density of the thiophene rings. However, further DFT calculations that are beyond the scope of this study are needed to support this interpretation.

Table 2. Fitting parameters of the deconvoluted contributions of the symmetric $C_{\alpha}C_{\beta}$ Raman signal of PEDOT:PSS, Te/PEDOT:PSS, and Ag_2Te /PEDOT:PSS samples. Different contributions correspond to different ECLs.

PEDOT:PSS	Center ^{a)} [cm ⁻¹]	1394.07	1411.73	1429.98	1441.68	1457.43
	fwhm [cm ⁻¹]	22.19	35.73	31.51	21.96	29.78
	I [a.u.]	0.12	0.34	0.69	0.18	0.17
	rel. I [%]	7.99	22.54	46.01	11.87	11.59
Te/PEDOT:PSS Pristine	Center [cm ⁻¹]	1399.66	1418.58	1427.23	1440.42	
	fwhm [cm ⁻¹]	33.22	16.76	18.27	21.41	
	rel. I [%]	12.42	27.05	51.56	8.97	
Te/PEDOT:PSS + H ₂ SO ₄	Center [cm ⁻¹]	1397.03	1424.18	1425.01	1443.21	1455.89
	fwhm [cm ⁻¹]	24.25	17.14	13.69	15.59	18.24
	I [a.u.]	0.05	0.79	0.16	0.04	0.10
	rel. I [%]	4.71	69.15	14.36	3.14	8.63
Te/PEDOT:PSS + EG	Center [cm ⁻¹]	1393.02	1425.84	1431.39	1454.52	
	fwhm [cm ⁻¹]	28.92	17.14	29.13	17.33	
	I [a.u.]	0.03	0.45	0.59	0.09	
	rel. I [%]	2.20	38.94	51.29	7.57	
Te/PEDOT:PSS + TDAE _(v)	Center [cm ⁻¹]	1396.95	1424.19	1445.92		
	fwhm [cm ⁻¹]	32.18	24.79	33.13		
	I [a.u.]	0.06	0.95	0.07		
	rel. I [%]	5.87	87.29	6.84		
Te/PEDOT:PSS + TDAE _(d)	Center [cm ⁻¹]	1397.59	1425.16	1453.53		
	fwhm [cm ⁻¹]	11.27	22.61	10.62		
	I [a.u.]	0.01	1	0.02		
	rel. I [%]	1.01	97.04	1.95		
Ag_2Te /PEDOT:PSS Pristine	Center [cm ⁻¹]	1395.40	1425.43	1456.93		
	fwhm [cm ⁻¹]	21.24	26.47	18.98		
	I [a.u.]	0.07	0.97	0.05		
	rel. I [%]	6.14	89.01	4.84		
Ag_2Te /PEDOT:PSS + H ₂ SO ₄	Center [cm ⁻¹]	1400.74	1426.32	1430.53	1455.24	
	fwhm [cm ⁻¹]	35.64	22.46	8.18	17.79	
	I [a.u.]	0.15	0.89	0.07	0.04	
	rel. I [%]	13.06	77.03	6.35	3.56	
Ag_2Te /PEDOT:PSS + EG	Center [cm ⁻¹]	1386.47	1402.53	1426.29	1454.45	
	fwhm [cm ⁻¹]	21.06	29.70	29.12	16.21	
	I [a.u.]	0.11	0.20	0.83	0.04	
	rel. I [%]	9.33	17.08	69.91	3.68	
Ag_2Te /PEDOT:PSS + TDAE _(v)	Center [cm ⁻¹]	1396.90	1427.26	1456.59		
	fwhm [cm ⁻¹]	16.43	24.20	22.77		
	I [a.u.]	0.05	0.98	0.03		
	rel. I [%]	4.46	92.62	2.92		
Ag_2Te /PEDOT:PSS + TDAE _(d)	Center [cm ⁻¹]	1426.72				
	fwhm [cm ⁻¹]	21.22				
	I [a.u.]	1.01				
	rel. I [%]	100				

^{a)}Keys: center, peak center; fwhm, full width at half maximum; I, intensity; a.u., arbitrary units; rel. I, relative intensity.

3.2. H₂SO₄ Post-Treatment

It has been reported that H₂SO₄ can effectively induce the phase segregation between PEDOT and PSS.^[66] It is known that concentrated H₂SO₄ undergoes autoprotolysis, where two H₂SO₄ molecules yield two ions: H₃SO₄⁺ and HSO₄⁻. These ions stabilize the segregated phases of the positively charged PEDOT and negatively charged PSS⁻, resulting in a more crystalline conformation of the obtained PEDOT-rich domains.^[24] Additionally, some of the protons generated after the dissociation of H₂SO₄ can be introduced into the thiophene backbone, thereby increasing the *h*⁺ concentration.^[67] When comparing *n* and *μ* with the *σ* and *S* variations of the Te/PEDOT:PSS sample post-treated with H₂SO₄, it is evident that the increased *n* is responsible for the increase in *σ* and the decrease in *S*. However, the explanation of the reduced *μ* is somewhat complicated, and the combination of HAXPES and Raman results is needed to understand it. From HAXPES measurements, it is possible to assume phase segregation and elimination of some excess PSS from the system, which would be ideally reflected as an improved crystallinity of the PEDOT-rich domains. Nevertheless, results from Raman measurements indicate that as the *n* increases due to the inclusion of protons into the thiophene backbone, the mixture of ECLs also increases, resulting in greater contributions in the short ECL region and therefore deteriorating the *π*-stacking of PEDOT chains and reducing *μ*. Nonetheless, the adverse effects of the reduction of *μ* on *σ* get nullified by the more significant increase of *n*.

For the Ag₂Te/PEDOT:PSS sample, there is also an increase of *n* with H₂SO₄ post-treatment, which is contrary to the expected results if the number of *h*⁺ is increased. In this case, we hypothesize that the H₂SO₄ post treatment causes the dissolution of AgO impurities present on the NWs (see Figure S26, Supporting Information) forming Ag⁺. This additional Ag⁺ can then enter the Ag₂Te lattice,^[68] increasing the overall concentration of interstitial Ag atoms, resulting in an increased concentration of *e*⁻ (*n*).^[13] In this case, the decreased PEDOT-to-PSS ratio also suggests a phase segregation between PEDOT and PSS. Similarly to the Te/PEDOT:PSS sample, the reduction of *μ* can be explained by the increased mixture of ECLs with contributions in the short ECL region, relative to the pristine sample, as found via Raman spectroscopy.

3.3. EG Post-Treatment

When Te/PEDOT:PSS and Ag₂Te/PEDOT:PSS are post-treated with EG, the PEDOT-to-PSS ratio is increased, indicating a removal of excess PSS. For Te/PEDOT:PSS, *n* remains unchanged and *μ* is decreased having a detrimental effect on *σ*. For the Ag₂Te/PEDOT:PSS, *n* is slightly increased and *μ* is reduced, but in this case, the electronic transport through the inorganic component has a more significant contribution to the overall *σ*, which is why the reduction of *μ* does not have a detrimental effect on the *σ*.^[13] The decrease in *μ* is surprising, since the phase segregation that is expected to accompany this post-treatment method normally results in an increase in *μ* for PEDOT-based materials.^[21] We hypothesize that the observed decrease of *μ* in our case is directly linked to

polymer morphology in the hybrid material. It has been found that PEDOT chains at the hybrid interface assemble with their *π*-structure against the inorganic material (i.e., the polymers lie flat). When the hybrid materials are post-treated with EG, there is a structural rearrangement of the polymer where the alignment of the polymer chains in the bulk-like PEDOT:PSS (thickness ≈6 nm, Figure S27, Supporting Information) that is not associated with the polymer layer at the hybrid interface is disrupted. Additionally, the assortment of ECLs for both samples and their increased FWHM indicate that the crystallinity of the lamellar domains is deteriorated,^[69] contributing to the reduction of the *μ* of the samples.

3.4. TDAE_(v) Post-Treatment

For the TDAE_(v) post-treatment, there are some fundamental differences between the effects on p-type Te/PEDOT:PSS and n-type Ag₂Te/PEDOT:PSS; nevertheless, we observe some trends that apply for both samples. In both cases, as the CT process takes place, the PEDOT:PSS portion of the hybrid gets reduced which is reflected as a decrease of the overall number of *h*⁺ present in PEDOT. For the p-type Te/PEDOT:PSS sample, this is reflected as a drop of *σ* and an increase of *S*. For the n-type Ag₂Te/PEDOT:PSS, the behavior is different. It appears to be a decrease of *n*, however, the observed differences are within error, making it difficult to draw any definitive conclusions regarding the effects on the *σ*. Nonetheless, the observed increase in *|S|* may be due to the reduction of *h*⁺ from PEDOT. As some of the *h*⁺ are removed from PEDOT after TDAE post-treatment, the total charge carrier density (*n*_t = *e*⁻ + *h*⁺) obtained from Hall measurements is slightly decreased. This has a positive effect on the *S* obtained, as its value is inversely proportional to *n*_t, (*π*/3*n*)^{2/3}. In both cases, *μ* is slightly increased suggesting that the TDAE_(v) post-treatment promotes the formation of lamellar domains, increasing the overall *σ*. Furthermore, the PEDOT-to-PSS ratio gets reduced, suggesting a phase segregation between PEDOT and PSS, and in both cases the contribution of different ECLs gets reduced and it appears to become homogenized toward one single ECL, as observed in the increased relative intensity of the main ECL shown in Table 2, having a positive effect on *μ*.

3.5. TDAE_(d) Post-Treatment

The effects of the TDAE_(d) post-treatment are similar to those of the TDAE_(v) for both samples. The *n* of Te/PEDOT:PSS sample is decreased by 99%, dropping its *σ* value close to those reported for Te/PVP.^[13] Additionally, its *S* was significantly increased to values close to those reported for pure Te with similar *n* values.^[70] For the Ag₂Te/PEDOT:PSS sample, similar to the TDAE_(v) post-treatment, there is a slight reduction of *n*, and the increase of *S* can also be explained by the reduction of *h*⁺ of PEDOT. In this case, the increase in *σ* can be explained by the pronounced increase of *μ* of ≈120%. Additionally, the PEDOT-to-PSS ratio gets reduced. We posit that the apparent increase of the PSS content for the TDAE treated samples is due to phase segregation between PEDOT and PSS. As TDAE

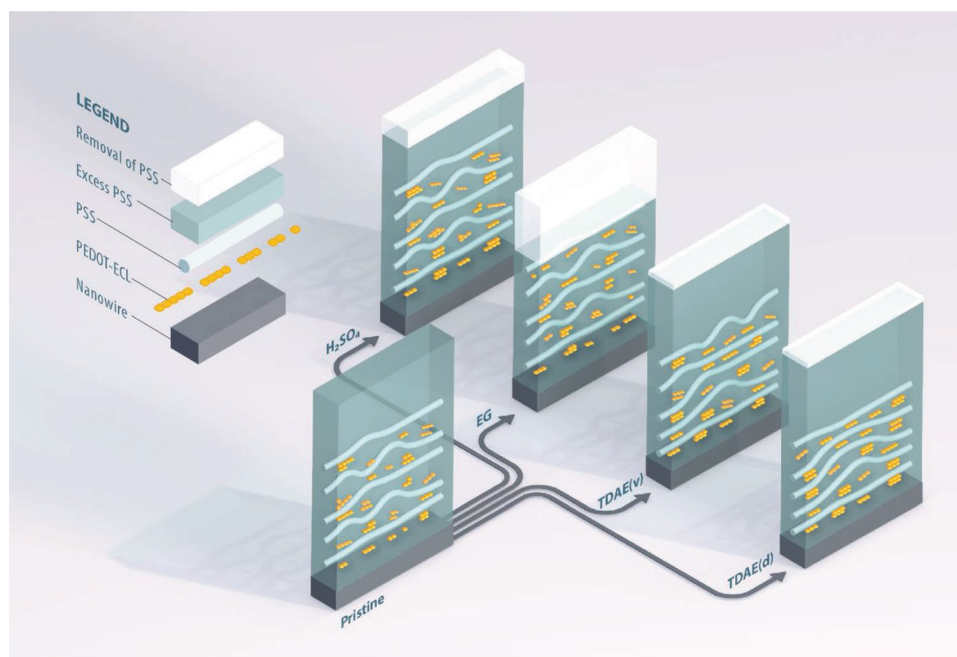


Figure 7. Schematic representation of the elicited effect of H_2SO_4 , EG, and TDAE post-treatments on the PEDOT:PSS component of Te/PEDOT:PSS and Ag_2Te /PEDOT:PSS hybrid materials. The PEDOT component is drawn in a way that it facilitates the visualization of different ECLs, and it does not represent PEDOT chains of different lengths.

reduces a part of PEDOT during the CT process, the excess portion of PSS gets segregated, and the oxidized TDAE^{2+} balances the charge of the sulfonate groups. In this case, the segregated PSS portion does not get washed away, decreasing the PEDOT-to-PSS ratio. The presence of TDAE on the post-treated samples is confirmed by the N 1s spectra (Figure S12b, Supporting Information), where the peak at 401.33 ± 0.05 eV corresponds to TDAE^{2+} .^[51] In the case of Te/PEDOT:PSS, the mixture of different ECLs is minimal and, for Ag_2Te /PEDOT:PSS, the ECL is completely homogenized as the Raman spectrum was deconvoluted to only one contribution. It is noteworthy to point out that the Ag_2Te /PEDOT:PSS post-treated with $\text{TDAE}_{(d)}$ presents the highest μ , strongly suggesting that the amount of different contributions in the Raman spectrum related to different ECLs plays an important role in the μ of the hybrids.

Figure 7 shows a schematic summary of the effects caused by the post-treatments on the PEDOT:PSS component of the hybrid materials, as unraveled by the combination of HAXPES and Raman analysis. It is noted that the structures depicted in this scheme are exaggerated and only express tendencies observed from experimental data.

4. Conclusion

In summary, we investigated the effects of primary doping through acid–base (A^+B^-) and CT processes using H_2SO_4 , and TDAE, respectively, as well as the effects of secondary doping by EG, on the TE performance of p-type Te/PEDOT:PSS and n-type Ag_2Te /PEDOT:PSS hybrids. Our results suggest that there are some primary differences between the EG post-treatment of pure PEDOT:PSS and Ag_xTe /PEDOT:PSS hybrid systems.

When the hybrid systems are post-treated with EG, which is one of the benchmark secondary dopants for increasing the σ of PEDOT:PSS, the morphological conformations of the PEDOT chains is disrupted, as opposed to the pure PEDOT:PSS systems where the morphological conformation of the chains is improved. This corrupts its lamellar domains by increasing the FWHM of ECLs affecting μ and deteriorating σ , thereby diminishing their overall TE performance. Post-treatment with H_2SO_4 greatly increases n through the insertion of protons into the PEDOT backbone; however, the tradeoff between enhancing σ and reducing S by boosting n results in a minimal improvement of the TE performance. $\text{TDAE}_{(d)}$ post-treatment proved to be more efficient than $\text{TDAE}_{(v)}$ post-treatment. The main differences rely on the effective diffusion of $\text{TDAE}_{(d)}$ into the samples, reducing the vast majority of the PEDOT component, eliminating the e^-h^+ interactions (for n-type systems), resulting in an increased $|S|$, and boosting the overall TE performance. Furthermore, we demonstrate how by analyzing the symmetric $C_{\alpha}C_{\beta}$ Raman signal of PEDOT:PSS, it is possible to estimate the number of different ECLs present in the system as well as their crystallinity, which plays an important role in the μ . Additionally, we provide evidence that strongly supports the direct experimental observation of the templating effect causing the planar alignment of the first few layers of PEDOT moieties over the Te and Ag_2Te NW surfaces.

Our work provides valuable insights into the mechanism of structural and electronic changes in hybrid organic–inorganic materials when different post-treatment procedures are applied, and highlights that in the case of EG post-treatment, the impact on pure polymer systems does not reflect the outcome for Ag_xTe /PEDOT:PSS hybrid systems. While this study focuses on PEDOT-based hybrid materials for thin film TEs,

these strategies are pertinent to other applications in the hybrid electronic materials community.

5. Experimental Section

Materials: All reagents were used as received unless otherwise noted. L-ascorbic acid ($C_6H_8O_6$), sodium tellurite (Na_2TeO_3), silver nitrate ($AgNO_3$), EG, sulfuric acid, PVP, and TDAE were procured from Sigma-Aldrich. PEDOT:PSS (branded as PH1000) was purchased from Ossila. All deionized (DI) water used for synthesis and purification was ultrapure ($>18\text{ M}\Omega\text{ cm}$).

Synthesis of Te/PEDOT:PSS Hybrid (1): Te/PEDOT:PSS was synthesized according to literature procedures.^[71] Briefly, ascorbic acid (1.908 g) was added into a 250 mL round bottom flask followed by the addition of DI H_2O (80 mL). The mixture was stirred at room temperature until the ascorbic acid was dissolved, at which point PEDOT:PSS (2 mL) previously filtered with a $0.45\ \mu\text{m}$ nylon syringe filter was added to the solution. Once a homogeneous blue solution was obtained, Na_2TeO_3 (0.1334 g) was added, and then the temperature was raised to $90\ ^\circ\text{C}$. When the reaction temperature reached $90\ ^\circ\text{C}$, the reaction vessel was plugged with a septum and allowed to react overnight ($\approx 16\text{ h}$). The solution was removed from heat and allowed to cool to room temperature before the second step of the synthesis.

Synthesis of Ag_2Te /PEDOT:PSS (2): For the chemical transformation of Te/PEDOT:PSS (1) to Ag_2Te /PEDOT:PSS hybrid material, the necessary amount of $AgNO_3$ to reach a molar ratio of Ag:Te of [2:1] was added at once to the room temperature ($\approx 23\ ^\circ\text{C}$) reaction (1) and allowed to react for 30 min with stirring. The resulting solution was centrifuged at 6000 rpm for 10 min, after which the supernatant was discarded. The residual solid was redispersed in DI H_2O with shaking and sonication, and subsequently centrifuged for a second time at 6000 rpm for 10 min. The second supernatant was discarded, and the residual solid material was redispersed in DI H_2O before processing into films for characterization.

Synthesis of Te/PVP: The Te/PVP reference material was synthesized according to the literature,^[72] in a similar method to that of the Te/PEDOT:PSS parent material, by replacing the PEDOT:PSS by PVP at a concentration of 20 g L^{-1} .

Synthesis of Ag /PEDOT:PSS: For the synthesis of Ag /PEDOT:PSS, ascorbic acid (1.908 g) was added into a 250 mL round bottom flask followed by the addition of DI H_2O (80 mL). The mixture was stirred at room temperature until the ascorbic acid was dissolved, at which point PEDOT:PSS (2 mL), previously filtered with a $0.45\ \mu\text{m}$ nylon syringe filter, was added to the solution. Once a homogeneous solution was formed, $AgNO_3$ (0.245 g) were added and allowed to react at room temperature ($\approx 23\ ^\circ\text{C}$) for 30 min. The resulting solution was centrifuged at 6000 rpm for 10 min, after which the supernatant was discarded. The residual solid was redispersed in DI H_2O with shaking and sonication, and subsequently centrifuged for a second time at 6000 rpm for 10 min. The second supernatant was discarded and the residual solid material was redispersed in DI H_2O .

Thin Film Fabrication: To make films for XRD characterization, concentrated solution of Te/PEDOT:PSS or Ag_2Te /PEDOT:PSS were drop casted onto $20 \times 20\text{ mm}^2$ clean glass and was heated at $120\ ^\circ\text{C}$ until completely dried. For Raman characterization, concentrated solutions were spin coated onto $20 \times 20\text{ mm}^2$ clean glass at 1k rpm for 60 s followed by annealing at $120\ ^\circ\text{C}$ for 2 min. This spin coating and annealing process was repeated twice.

To make films for the thermoelectric characterization, concentrated solutions were spin coated onto Linseis Thin Film Analyzer (TFA) chips at 1k rpm for 60 s followed by annealing at $120\ ^\circ\text{C}$ for 2 min. This spin coating and annealing process was repeated four times to ensure homogeneous and sufficiently thick films for characterization.

For HAXPES characterization, concentrated solutions were spin coated onto $10 \times 10\text{ mm}$ clean indium tin oxide-coated glass substrates at 1k rpm for 60 s followed by annealing at $120\ ^\circ\text{C}$ for 2 min. This spin coating and annealing process was repeated twice.

Thin films for all characterization techniques were processed under ambient conditions.

Thin Film Post-Treatment: For the post-treatment with TDAE vapor ($TDAE_{(v)}$), $\approx 50\ \mu\text{L}$ of TDAE were deposited on the bottom of a petri dish, the samples were taped to the top lid, and then the petri dish was closed and left under nitrogen atmosphere for 15 min to ensure the evaporation of TDAE. For the post-treatment with TDAE drop ($TDAE_{(d)}$), enough TDAE droplets were added into the samples to ensure a full coverage of the surface and were left to react for two minutes under nitrogen atmosphere. For the post-treatment with EG, samples were fully submerged into EG for 30 min. For the post-treatment with H_2SO_4 , samples were fully submerged into H_2SO_4 (14.7 m) solution for 10 min. After all of the post-treatment methods, the samples were washed in a water bath to remove the excess of TDAE, EG or H_2SO_4 present on the films, then they were annealed at $120\ ^\circ\text{C}$ for 2 min. Thin films fabricated for different characterization techniques were subjected to the same post-treatment procedures.

Structural and Morphological Characterization: XRD measurements were carried out in the X-Ray Core-Lab at Helmholtz-Zentrum Berlin (HZB) on a Bruker D8 X-ray powder diffractometer (XRD) in Bragg-Brentano geometry, equipped with a LynxEye detector, and using $Cu\ K\alpha_{1+2}$ radiation. All data have been analyzed with DiffracEVA software using the The International Centre for Diffraction Data PDF4+ database.

Raman spectroscopy measurements were performed on a Micro-Raman system LabRam microscope (100x objective) from Dilor with an excitation wavelength of 632.8 nm from a He-Ne laser. The deconvolution of the Raman spectra was done using Origin 2019 software with a Lorentzian line shape without applying any constraints to the peak center and linewidth, i.e., FWHM. The peak center was left without a position constraint since its position shifts depending on the ECL. In a similar manner, no constraint for the FWHM was used since its value changes as the crystallinity of the lamellar domains is modified, where small FWHM corresponds to higher crystallinity of the lamellar domains, and vice versa.^[69]

TEM was carried out at the Bundesanstalt für Materialforschung und -prüfung (BAM) in the structure analysis division on a Thermo Scientific Talos Arctica 200 kV field emission gun TEM. All TEM samples were prepared by drop casting dilute dispersions of the hybrid material from DI H_2O onto 200 mesh copper TEM grids coated with ultrathin carbon and lacey carbon support films (PLANO, GmbH). All TEM image analysis was carried out using ImageJ software.^[73]

Thickness measurements were performed using a Dektak XT stylus profilometer on the step edge of both sides of the prepared thin films. A statistical distribution fit was performed on the measured location along the thin-films deposited on the TFA chips, the obtained median was used as the thickness value and the corresponding median absolute deviation was propagated through the error analysis as detailed for the thermoelectric characterization.

HAXPES: HAXPES measurements were conducted at the HiKE endstation located at the Berliner Elektronenspeicherring-Gesellschaft für Synchrotronstrahlung II KMC-1 beamline at HZB.^[74,75] To prevent beam-damage degradation of the organic component of the investigated samples, the HAXPES experimental campaign was conducted during a single bunch mode week, during which BESSY II operates with a ring current of 13 mA (compared to a ring current of 300 mA for standard multibunch beam). The HAXPES measurements were performed in an ultrahigh vacuum chamber ($<1 \times 10^{-8}\text{ mbar}$) using a Scienta R4000 electron analyzer and 3 keV excitation. This experimental setup allowed for measurements of the Ag 3p/Te 3d, O 1s, N 1s, Ag 3d, and C 1s core levels with photoelectron inelastic mean free path values (IMFP, which describes the exponential attenuation of photoelectrons travelling through matter) of $\approx 6\text{ nm}$ through the organic components (i.e., PEDOT:PSS) of the materials, as calculated by the Tanuma, Powell, Penn 2 Method (TPP-2M) formula using the Quases-Tourgaard code.^[76,77] In this case, IMFP represents the material thickness required to attenuate the photoelectron signal to a factor of $1/e \approx 0.36$. Thus, 95% of the signal is attenuated when the photoelectrons come from a depth equal to $3 \times$ IMFP [also known as measurement information depth (ID)]. For the measurements of the S 1s

core level, due to its higher BE, S 1s photoelectrons exhibit substantially lower kinetic energy and, therefore, a reduced IMFP (i.e., ≈ 2 nm, resulting in an ID of ≈ 6 nm). Nevertheless, based on TEM derived thickness of the PEDOT:PSS coating layers (see Figure S27, Supporting Information), the IDs of the performed HAXPES measurements are sufficient to probe the chemical properties of the organic layers, the organic/inorganic interface, and even the buried inorganic nanowires. The energy scale of the HAXPES measurements was calibrated using Au 4f reference spectra of a clean Au foil, setting the BE of the Au 4f_{7/2} line to 84.00 eV. Curve fit analysis of the measured detail HAXPES spectra were simultaneously conducted with the Fityk software.^[78] Voigt profile functions and linear backgrounds were mostly used for these fits. [The only exception to this criterion was made for the thiophene contribution of the S 1s spectra (i.e., thiophene peak), which exhibits an asymmetric line shape resulting from positive charge delocalization in the PEDOT polymer;^[47,79] in this case, a Doniach-Sunjić function was used]. Spin-orbit doublets were fit using two Voigt functions with intensity ratios set to obey the $2j + 1$ multiplicity rule. HAXPES-derived [Ag]:[Te] composition ratio quantifications were carried out by correcting the peak intensities of the Ag 3p_{3/2} and Te 3d_{5/2} HAXPES core levels to account for differences in photoionization cross-section.^[80] Due to the energetic proximity of these lines, the impact of differences in IMFP^[76,77] and the transmission function of the electron analyzer^[81] on the intensity of the core levels is negligible.

Thermoelectric Characterization: The measurements of electrical conductivity (σ), Seebeck coefficient (S), thermal conductivity (κ), Hall carrier density (n), and Hall carrier mobility (μ) were performed on a Linseis TFA. The test TFA chips used for the measurements combine a setup of two suspended Si₃N₄ membranes, based on the 3 ω -Völklein geometry for the in-plane thermal conductivity measurements and a 4-contact Van der Pauw measurement setup for the determination of the electrical transport properties. The magnetic field used for the Hall measurements was 0.50 T, and the measurements were performed at 20 °C. The Seebeck coefficient is measured using a partly passivated resistance thermometer, located on top of the large Si₃N₄ membrane. A detailed description of the measurement techniques employed can be found in references.^[82,83] All samples were subjected to two heating-cooling cycles between 20 and 120 °C. All properties were measured every 10 °C, and the heating/cooling rate was of 10 °C min⁻¹.

All shown uncertainties for σ , S , κ , n , and μ take into consideration the error percentage for the current, voltage, temperature, and magnetic field given by the manufacturer. Additionally, the errors for σ , κ , n , and μ include the thickness error added by means of Gaussian error propagation.

Supporting Information

Supporting Information is available from the Wiley Online Library or from the author.

Acknowledgements

The authors would like to acknowledge the BAM Division 6.3 for structure analysis, in particular Carsten Prinz and Dr. Franziska Emmerling for access to and support with the TEM. The authors thank HZB for access to synchrotron radiation beamtime for HAXPES experiments. Finally, the authors thank Alexander Steigert for assistance during the beamtime.

Open access funding enabled and organized by Projekt DEAL.

Conflict of Interest

The authors declare no conflict of interest.

Data Availability Statement

The data that support the findings of this study are available from the corresponding author upon reasonable request.

Keywords

hybrid materials, PEDOT:PSS, post-treatment, silver telluride, tellurium, thin film thermoelectric

Received: February 27, 2023

Published online:

- [1] B. Meng, J. Liu, L. Wang, *Nano Mater. Sci.* **2021**, *3*, 113.
- [2] M. Goel, M. Thelakkat, *Macromolecules* **2020**, *53*, 3632.
- [3] C. J. Yao, H. L. Zhang, Q. Zhang, *Polymers* **2019**, *11*, 107.
- [4] Y. Sun, C. A. Di, W. Xu, D. Zhu, *Adv. Electron. Mater.* **2019**, *5*, 1800825.
- [5] Y. Lu, J. Y. Wang, J. Pei, *Chem. Mater.* **2019**, *31*, 6412.
- [6] A. Marks, X. Chen, R. Wu, R. B. Rashid, W. Jin, B. D. Paulsen, M. Moser, X. Ji, S. Griggs, D. Meli, X. Wu, H. Bristow, J. Strzalka, N. Gasparini, G. Costantini, S. Fabiano, J. Rivnay, I. McCulloch, *J. Am. Chem. Soc.* **2022**, *144*, 4642.
- [7] G. J. Snyder, E. S. Toberer, *Nat. Mater.* **2008**, *7*, 105.
- [8] N. E. Coates, S. K. Yee, B. McCulloch, K. C. See, A. Majumdar, R. A. Segalman, J. J. Urban, *Adv. Mater.* **2013**, *25*, 1629.
- [9] X. Zhang, S. Pan, H. Song, W. Guo, S. Zhao, G. Chen, Q. Zhang, H. Jin, L. Zhang, Y. Chen, S. Wang, *Front. Chem.* **2021**, *9*, 273.
- [10] P. Kumar, E. W. Zaia, E. Yildirim, D. V. M. Repaka, S.-W. Yang, J. J. Urban, K. Hippalgaonkar, *Nat. Commun.* **2018**, *9*, 5347.
- [11] S. K. Yee, N. E. Coates, A. Majumdar, J. J. Urban, R. A. Segalman, *Phys. Chem. Chem. Phys.* **2013**, *15*, 4024.
- [12] E. W. Zaia, A. Sahu, P. Zhou, M. P. Gordon, J. D. Forster, S. Aloni, Y.-S. Liu, J. Guo, J. J. Urban, *Nano Lett.* **2016**, *16*, 3352.
- [13] K. A. Mazzio, D. Kojda, R. Rubio-Govea, J. Niederhausen, B. Ryll, M. Raja-Thulasimani, K. Habicht, S. Raoux, *ACS Appl. Energy Mater.* **2020**, *3*, 10734.
- [14] O. Bubnova, Z. U. Khan, A. Malti, S. Braun, M. Fahlman, M. Berggren, X. Crispin, *Nat. Mater.* **2011**, *10*, 429.
- [15] H. Wang, J. H. Hsu, S. I. Yi, S. L. Kim, K. Choi, G. Yang, C. Yu, *Adv. Mater.* **2015**, *27*, 6855.
- [16] Y. Zheng, H. Zeng, Q. Zhu, J. Xu, *J. Mater. Chem. C* **2018**, *6*, 8858.
- [17] S. Shin, J. W. Roh, H. S. Kim, R. Chen, *J. Appl. Phys.* **2018**, *123*, 205106.
- [18] Y. Liu, P. Liu, Q. Jiang, F. Jiang, J. Liu, G. Liu, C. Liu, Y. Du, J. Xu, *Chem. Eng. J.* **2021**, *405*, 126510.
- [19] I. Zozoulenko, A. Singh, S. K. Singh, V. Gueskine, X. Crispin, M. Berggren, *ACS Appl. Polym. Mater.* **2019**, *1*, 83.
- [20] M. Donova, M. Micjan, M. Novota, J. Nevrela, S. Kovacova, M. Pavuk, P. Juhasz, M. Jagelka, J. Kovac, J. Jakabovic, M. Cigan, M. Weis, *Appl. Surf. Sci.* **2017**, *395*, 86.
- [21] K. Itoh, Y. Kato, Y. Honma, H. Masunaga, A. Fujiwara, S. Iguchi, T. Sasaki, *J. Phys. Chem. C* **2019**, *123*, 13467.
- [22] W. Zhao, J. Ding, Y. Zou, C. A. Di, D. Zhu, *Chem. Soc. Rev.* **2020**, *49*, 7210.
- [23] Z. Fan, J. Ouyang, *Adv. Electron. Mater.* **2019**, *5*, 1800769.
- [24] N. Kim, S. Kee, S. H. Lee, B. H. Lee, Y. H. Kahng, Y. R. Jo, B. J. Kim, K. Lee, *Adv. Mater.* **2014**, *26*, 2268.
- [25] A. M. Glauddell, J. E. Cochran, S. N. Patel, M. L. Chabincyn, *Adv. Energy Mater.* **2015**, *5*, 1401072.

- [26] L. Zhang, K. Yang, R. Chen, Y. Zhou, S. Chen, Y. Zheng, M. Li, C. Xu, X. Tang, Z. Zang, K. Sun, *Adv. Electron. Mater.* **2020**, *6*, 1900648.
- [27] M. N. Gueye, A. Carella, J. Faure-Vincent, R. Demadrille, J. P. Simonato, *Prog. Mater. Sci.* **2020**, *108*, 100616.
- [28] O. Bubnova, X. Crispin, *Energy Environ. Sci.* **2012**, *5*, 9345.
- [29] G. Zotti, A. S. Zecchin, G. Schiavon, F. L. And, L. Groenendaal, X. Crispin, A. W. Osikowicz, W. Salaneck, M. Fahlman, *Macromolecules* **2003**, *36*, 3337.
- [30] S. K. M. Jönsson, J. Birgersson, X. Crispin, G. Greczynski, W. Osikowicz, A. W. Denier van der Gon, W. R. Salaneck, M. Fahlman, *Synth. Met.* **2003**, *139*, 1.
- [31] X. Crispin, S. Marciniak, W. Osikowicz, G. Zotti, A. W. Denier Van Der Gon, F. Louwet, M. Fahlman, L. Groenendaal, F. De Schryver, W. R. Salaneck, *J. Polym. Sci., Part B: Polym. Phys.* **2003**, *41*, 2561.
- [32] P. V. Almeida, C. M. S. Izumi, H. F. Dos Santos, A. C. Sant'Ana, *Quim. Nova* **2019**, *42*, 1073.
- [33] S. Garreau, G. Louarn, J. P. Buisson, A. G. Froyer, S. Lefrant, *Macromolecules* **1999**, *32*, 6807.
- [34] J. Ouyang, Q. Xu, C.-W. Chu, Y. Yang, G. Li, J. Shinar, *Polymer* **2004**, *45*, 8443.
- [35] W. W. Chiu, J. Travaš-Sejdić, R. P. Cooney, G. A. Bowmaker, *Synth. Met.* **2005**, *155*, 80.
- [36] W. W. Chiu, J. Travaš-Sejdić, R. P. Cooney, G. A. Bowmaker, *J. Raman Spectrosc.* **2006**, *37*, 1354.
- [37] J. Ouyang, C. W. Chu, F. C. Chen, Q. Xu, Y. Yang, *Adv. Funct. Mater.* **2005**, *15*, 203.
- [38] E. Hosseini, V. Ozhukil Kollath, K. Karan, *J. Mater. Chem. C* **2020**, *8*, 3982.
- [39] N. A. Shahrim, Z. Ahmad, A. W. Azman, Y. F. Buys, N. Sarifuddin, *Mater. Adv.* **2021**, *2*, 7118.
- [40] Y. Xu, Y. Jia, P. Liu, Q. Jiang, D. Hu, Y. Ma, *Chem. Eng. J.* **2021**, *404*, 126552.
- [41] S. Wang, G. Zuo, J. Kim, H. Siringhaus, *Prog. Polym. Sci.* **2022**, *129*, 101548.
- [42] L. Yang, M. P. Gordon, A. K. Menon, A. Bruefach, K. Haas, M. C. Scott, R. S. Prasher, J. J. Urban, *Sci. Adv.* **2021**, *7*, eabe6000.
- [43] Linseis Messgeraete GmbH, <https://www.linseis.com/en/products/thin-film-analyzer/tfa-thin-film-analyzer/#Specifications> (accessed: April 2022).
- [44] T. S. Sreepasad, A. K. Samal, T. Pradeep, *Chem. Mater.* **2009**, *21*, 4527.
- [45] J. F. Moulder, *Handbook of X-Ray Photoelectron Spectroscopy: A Reference Book of Standard Spectra for Identification and Interpretation of XPS Data* (Ed: J. Chastain), Physical Electronics Division, Perkin-Elmer Corporation, Minnesota, USA **1992**.
- [46] N. Kumar, S. Sinha Ray, J. C. Ngila, *New J. Chem.* **2017**, *41*, 14618.
- [47] S. Jäckle, M. Liebhaber, J. Niederhausen, M. Büchele, R. Félix, R. G. Wilks, M. Bär, K. Lips, S. Christiansen, *ACS Appl. Mater. Interfaces* **2016**, *8*, 8841.
- [48] K. Okamoto, Y. Abe, S. Ueda, *Hyomen Kagaku* **2016**, *37*, 386.
- [49] J. Zillner, H.-G. Boyen, P. Schulz, J. Hanisch, N. Gauquelin, J. Verbeeck, J. Küffner, D. Desta, L. Eisele, E. Ahlswede, M. Powalla, *Adv. Funct. Mater.* **2022**, *32*, 2109649.
- [50] M. A. Bryant, J. E. Pemberton, *J. Am. Chem. Soc.* **1991**, *113*, 3629.
- [51] L. Lindell, A. Burquel, F. L. E. Jakobsson, V. Lemaur, M. Berggren, R. Lazzaroni, J. Cornil, W. R. Salaneck, X. Crispin, *Chem. Mater.* **2006**, *18*, 4246.
- [52] D. McGillivray, J. P. Thomas, M. Abd-Ellah, N. F. Heinig, K. T. Leung, *ACS Appl. Mater. Interfaces* **2016**, *8*, 34303.
- [53] M. Łapkowski, A. Proń, *Synth. Met.* **2000**, *110*, 79.
- [54] E. Agosti, M. Rivola, V. Hernandez, M. Del Zoppo, G. Zerbi, *Synth. Met.* **1999**, *100*, 101.
- [55] C. M. Castro, M. C. R. Delgado, V. Hernández, S. Hotta, J. Casado, J. T. López Navarrete, *J. Chem. Phys.* **2002**, *116*, 10419.
- [56] R. P. Ortiz, J. Casado, S. R. González, V. Hernández, J. T. López Navarrete, P. M. Viruela, E. Ortí, K. Takimiya, T. Otsubo, *Chem. - Eur. J.* **2010**, *16*, 470.
- [57] A. Milani, L. Brambilla, M. Del Zoppo, G. Zerbi, *J. Phys. Chem. B* **2007**, *111*, 1271.
- [58] S. R. González, Y. Ie, Y. Aso, J. T. López Navarrete, J. Casado, *J. Am. Chem. Soc.* **2011**, *133*, 16350.
- [59] J. Casado, L. L. Miller, K. R. Mann, T. M. Pappenfus, V. Hernández, J. T. López Navarrete, *J. Phys. Chem. B* **2002**, *106*, 3597.
- [60] J. Casado, K. Takimiya, T. Otsubo, F. J. Ramírez, J. Joaquín Quirante, R. Ponce Ortiz, S. R. González, M. Moreno Oliva, J. T. López Navarrete, *J. Am. Chem. Soc.* **2008**, *130*, 14028.
- [61] M. Stavtyska-Barba, A. M. Kelley, *J. Phys. Chem. C* **2010**, *114*, 6822.
- [62] F. Tran-Van, S. Garreau, G. Louarn, G. Froyer, C. Chevrot, *Synth. Met.* **2001**, *119*, 381.
- [63] P. J. Donohoo-Vallett, A. E. Bragg, *J. Phys. Chem. B* **2015**, *119*, 3583.
- [64] H. Vázquez, Y. J. Dappe, J. Ortega, F. Flores, *J. Chem. Phys.* **2007**, *126*, 144703.
- [65] J. Niederhausen, K. A. Mazzio, R. W. MacQueen, *Electron. Struct.* **2021**, *3*, 033002.
- [66] L. Bießmann, N. Saxena, N. Hohn, M. A. Hossain, J. G. C. Veinot, P. Müller-Buschbaum, *Adv. Electron. Mater.* **2019**, *5*, 1800654.
- [67] E. Jin Bae, Y. Hun Kang, K. S. Jang, S. Yun Cho, *Sci. Rep.* **2016**, *6*, 18805.
- [68] M. Shiojiri, T. Isshiki, Y. Hirota, K. Okashita, *Bull. Inst. Chem. Res., Kyoto Univ.* **1989**, *66*, 517.
- [69] W. C. Tsoi, D. T. James, J. S. Kim, P. G. Nicholson, C. E. Murphy, D. D. C. Bradley, J. Nelson, J. S. Kim, *J. Am. Chem. Soc.* **2011**, *133*, 9834.
- [70] S. Lin, W. Li, Z. Chen, J. Shen, B. Ge, Y. Pei, *Nat. Commun.* **2016**, *7*, 10287.
- [71] K. C. See, J. P. Feser, C. E. Chen, A. Majumdar, J. J. Urban, R. A. Segalman, *Nano Lett.* **2010**, *10*, 4664.
- [72] C. D. Brown, D. M. Cruz, A. K. Roy, T. J. Webster, *J. Nanopart. Res.* **2018**, *20*, 254.
- [73] C. A. Schneider, W. S. Rasband, K. W. Eliceiri, *Nat. Methods* **2012**, *9*, 671.
- [74] F. Schaefers, M. Mertin, M. Gorgoi, *Rev. Sci. Instrum.* **2007**, *78*, 123102.
- [75] M. Gorgoi, S. Svensson, F. Schäfers, G. Öhrwall, M. Mertin, P. Bressler, O. Karis, H. Siegbahn, A. Sandell, H. Rensmo, W. Doherty, C. Jung, W. Braun, W. Eberhardt, *Nucl. Instrum. Methods Phys. Res., Sect. A* **2009**, *601*, 48.
- [76] S. Tanuma, C. J. Powell, D. R. Penn, *Surf. Interface Anal.* **1994**, *21*, 165.
- [77] S. Tougaard, *QUASES-IMFP-TPP2M Program*, Quases-Tougaard Inc., Odense, Denmark **2002**.
- [78] M. Wojdyr, *J. Appl. Crystallogr.* **2010**, *43*, 1126.
- [79] G. Greczynski, T. Kugler, M. Keil, W. Osikowicz, M. Fahlman, W. R. Salaneck, *J. Electron Spectrosc. Relat. Phenom.* **2001**, *121*, 1.
- [80] M. B. Trzhaskovskaya, V. I. Nefedov, V. G. Yarzhevsky, *At. Data Nucl. Data Tables* **2001**, *77*, 97.
- [81] M. P. Seah, G. C. Smith, *Surf. Interface Anal.* **1990**, *15*, 751.
- [82] V. Linseis, F. Völklein, H. Reith, P. Woias, K. Nielsch, *J. Mater. Res.* **2016**, *31*, 3196.
- [83] V. Linseis, Z. M. Hassan, H. Reith, J. Garcia, K. Nielsch, H. Baumgart, E. Redel, P. Woias, *Phys. Status Solidi A* **2018**, *215*, 1700930.